

Tests of core flow imaging methods with numerical dynamos

Hagay Amit,^{1*} Peter Olson¹ and Ulrich Christensen²

¹Department of Earth and Planetary Sciences, Johns Hopkins University, Baltimore, MD 21218, USA

²Max-Planck-Institut für Sonnensystemforschung, 37191 Katlenburg-Lindau, Germany

Accepted 2006 August 4. Received 2006 April 26; in original form 2005 October 20

SUMMARY

We test the quality of a new core flow imaging method that incorporates constraints on flow helicity, using synthetic magnetic secular variation data from 3-D self-consistent numerical dynamo models. Comparison with the dynamo model flows reveals that our imaging method delineates most of the main large-scale flow features, both in pattern and magnitude. The dynamo model flows are characterized by high-latitude vortices, some equatorial symmetry, columnar convection and a significant amount of flow along radial magnetic field contours. Our inversion method correctly images these aspects of the flows. The correlation coefficient between the dynamo velocity and the imaged velocity exceeds 0.5 in cases with large-scale flow and magnetic field pattern, but degrades substantially in more complex cases when the scale of the secular variation is small. The magnitude of the imaged velocity depends on the *a priori*-assumed ratio of tangential divergence to radial vorticity k , in some resemblance to the damping parameter in spectral methods, although with our method the misfit is insensitive to k -values. Including tangential magnetic diffusion in core flow inversion improves the quality of the imaged velocity pattern. The largest artefacts in the imaged velocities are due to unmodelled radial magnetic diffusion and truncation of the input magnetic field.

Key words: core flow, dynamo theory, geomagnetic secular variation, magnetic diffusion.

1 INTRODUCTION

Images of fluid motion at the top of the Earth's outer core have been obtained by inverting geomagnetic secular variation data using the assumption of frozen magnetic flux (e.g. Gire *et al.* 1986; Voorhies 1986; Bloxham 1989; Gire & LeMouél 1990; Bloxham & Jackson 1991; Jackson *et al.* 1993; Pais & Hulot 2000; Holme & Whaler 2001; Hulot *et al.* 2002; Amit & Olson 2004, 2006). These inversions provide the most detailed images of core flow available, although they suffer from several problems, including unmodelled magnetic diffusion, data truncation, oversimplified assumptions for the tangential divergence of the core flow and non-uniqueness, all of which contribute to core flow models that substantially differ from each other.

The differences between core flow models obtained from the same secular variation data indicate the need for objective testing. Rau *et al.* (2000) proposed a core flow imaging test using synthetic secular variation data produced from 3-D self-consistent magnetohydrodynamic dynamo models. They compared the actual flow from a dynamo model with its image, obtained by inverting the magnetic secular variation of the same dynamo model. Rau *et al.* (2000) assumed tangential geostrophy or toroidal flow, and succeeded in imaging most of the main features of the dynamo model flow.

However, their results highlighted several problems with the inversion; specifically, they obtained the correct flow magnitude only by increasing the data misfit, they found unmodelled magnetic diffusion effects contaminate the flow pattern in places and flow artefacts were present due to data truncation effects. Here we follow the procedure of Rau *et al.* (2000) and test our core flow imaging method using the output of numerical dynamo models, by comparing the imaged velocity with the actual dynamo velocity.

We use the new core flow inversion method proposed by Amit & Olson (2004) that is based on the kinematics of flow seen in numerical dynamo models. They assumed that the tangential divergence of the flow is a superposition of two effects, the conventional tangential geostrophy effect (e.g. LeMouél 1984) plus a second term in which the tangential divergence is correlated with the radial vorticity, which they call helical flow. Helical flow kinematics are found in a variety of rotating–convecting flows as shown in analytical examples (Amit & Olson 2004) and are present in numerical dynamos (Olson *et al.* 2002). The helical flow assumption adds streamfunction diffusion to the induction equation and permits a solution of a set of partial differential equations for the flow potentials on a finite-difference grid.

2 THE FORWARD PROBLEM: NUMERICAL DYNAMO MODELS

The forward problem we consider consists of a numerical solution to a set of dynamically self-consistent dynamo equations. We solve

*Now at: IPGP, France. E-mail: hagay@ipgp.jussieu.fr

Table 1. Dynamo model calculations. Ra , Ek , Pr and P_m are the (modified) Rayleigh, Ekman, Prandtl and magnetic Prandtl numbers, respectively. T_{cmb} denotes the type of thermal boundary condition applied on the outer boundary. l_{max} is the maximal spherical harmonic, and N_r is the number of radial grid points. d_{ref} is the depth (in units of core radius) where the dynamo velocity is evaluated. Δt is the time difference (in units of viscous diffusion time) between the two B_r snapshots from which the average magnetic field and the difference secular variation are calculated. The magnetic Reynolds number R_m is calculated by averaging the dynamo velocity in volume and time, where the core radius is taken as a length-scale. In the scale-dependent magnetic Reynolds number R_m^* the length is derived from the magnetic power spectrum (see text for details). The correlation coefficient between $\nabla_h \cdot \vec{u}_h^*$ and $\mp \zeta^*$ is c_h^* , and their proportionality obtained by an areal-averaged linear fit regression is k^* .

	Case 1	Case 2	Case 3	Case 4
Ra	3e5 (5.4 Ra_{crit})	2.4e5 (4.3 Ra_{crit})	1.5e7 (22 Ra_{crit})	1.5e7 (22 Ra_{crit})
Ek	1e-3	1e-3	1e-4	1e-4
Pr	1	1	1	1
P_m	4	3	2	2
T_{cmb}	Isothermal	Isothermal	Uniform heat flux	Tomographic
l_{max}	53	42	85	85
N_r	33	33	41	41
d_{ref}	0.03834	0.03834	0.02474	0.02474
Δt	16.975e-4	4.00066e-3	10.1060e-5	9.29280e-5
R_m	111	70	319	314
R_m^*	145	122	189	195
c_h^*	0.83	0.85	0.50	0.48
k^*	0.31	0.29	0.13	0.11

the following non-dimensional Boussinesq magnetohydrodynamics equations for dynamo action due to thermal convection of an electrically conducting fluid in a rotating spherical shell (e.g. Olson *et al.* 1999).

$$Ek \left(\frac{\partial \vec{u}}{\partial t} + \vec{u} \cdot \nabla \vec{u} - \nabla^2 \vec{u} \right) + 2\hat{z} \times \vec{u} + \nabla P = Ra \frac{\vec{r}}{R} T + \frac{1}{P_m} (\nabla \times \vec{B}) \times \vec{B}, \quad (1)$$

$$\frac{\partial \vec{B}}{\partial t} = \nabla \times (\vec{u} \times \vec{B}) + \frac{1}{P_m} \nabla^2 \vec{B}, \quad (2)$$

$$\frac{\partial T}{\partial t} + \vec{u} \cdot \nabla T = \frac{1}{Pr} \nabla^2 T, \quad (3)$$

$$\nabla \cdot \vec{u} = 0, \quad (4)$$

$$\nabla \cdot \vec{B} = 0, \quad (5)$$

where \vec{u} is the velocity, \vec{B} is the magnetic field, T is temperature, t is time, \hat{z} is a unit vector in the direction of the rotation axis, P is pressure and \vec{r} is the position vector. Four non-dimensional parameters in eqs (1)–(5) control the dynamo action. The (modified) Rayleigh number represents the strength of buoyancy force driving the convection

$$Ra = \frac{\alpha g_0 \Delta T D}{\nu \Omega}, \quad (6)$$

where α is thermal expansivity, g_0 is gravitational acceleration on the outer boundary at radius R , ΔT is temperature difference between the inner and outer boundaries, D is shell thickness, ν is kinematic viscosity and Ω is rotation rate. The Ekman number represents the

ratio of viscous and Coriolis forces

$$Ek = \frac{\nu}{\Omega D^2}, \quad (7)$$

the Prandtl number is the ratio of kinematic viscosity to thermal diffusivity κ

$$Pr = \frac{\nu}{\kappa}, \quad (8)$$

and the magnetic Prandtl number is the ratio of kinematic viscosity to magnetic diffusivity λ

$$P_m = \frac{\nu}{\lambda}. \quad (9)$$

We selected four cases from two large systematic parameter space studies (Christensen *et al.* 1999; Olson & Christensen 2002). Table 1 summarizes the parameters, boundary conditions, numerical resolution and the reference depth that represents the free stream velocity below the Ekman boundary layer in the four cases we examined. In all cases the boundaries are rigid, the regions outside the shell are electrical insulators, and the inner boundary temperature is fixed. The outer boundary has fixed temperature in cases 1 and 2, fixed uniform heat flux in case 3, and heterogeneous heat flux proportional to the lowermost mantle S -wave seismic tomography model of Masters *et al.* (1996) in case 4. Cases 1 and 2 have a lower numerical resolution than cases 3 and 4. In all cases the dipole mode dominates the magnetic energy spectrum on the outer boundary and a significant secular variation is present.

From the numerical dynamo output we construct synthetic magnetic field and secular variation data to test our core flow imaging method, as follows. We sampled the model output after each dynamo simulation reached a state of statistical equilibrium, that is, the magnetic and kinetic energies fluctuated chaotically but without a trend. The secular variation data were constructed by finite differencing the radial component of the magnetic field B_r on the outer boundary grid points using two successive snapshots at times t and

$t + \Delta t$ to produce $\partial B_r / \partial t$. The data for the radial magnetic field were constructed by averaging the two snapshots on the same grid. Snapshots of the tangential velocity field at the reference depth d_{ref} taken at the same times were averaged to form \vec{u}_h^* , hereafter called the *dynamo velocity*.

There is some freedom in the choice of reference depth for the dynamo velocity. Due to computational limitations, numerical dynamos use an Ekman number larger than appropriate for the core, and therefore the Ekman boundary layer in the dynamo models is thicker than in the core. However, since the magnetic boundary layer in the model is thicker than the Ekman boundary layer (Rau *et al.* 2000), we adopt the self-consistent procedure of computing the secular variation at the outer boundary and the dynamo velocity at the top of the free stream below the Ekman boundary layer.

3 THE INVERSE PROBLEM: IMAGING METHOD

The inverse method commonly used to extract information on core motions from geomagnetic secular variation data (Gubbins 2004) consists of substituting the radial magnetic field B_r and secular variation $\partial B_r / \partial t$ obtained from the solution to the forward problem into the radial component of the magnetic induction eq. (2) and inverting for \vec{u}_h , which we refer to as the *imaged velocity*. The radial component of eq. (2) just below the outer boundary (where radial velocity is negligible) is

$$\frac{\partial B_r}{\partial t} + \vec{u}_h \cdot \nabla B_r + B_r \nabla_h \cdot \vec{u}_h = \frac{1}{P_m} \left(\frac{1}{R^2} \frac{\partial^2}{\partial r^2} (r^2 B_r) + \nabla_h^2 B_r \right) \quad (10)$$

where r is the radial coordinate, R is the outer boundary radius and $\nabla_h^2 = \nabla^2 - \frac{1}{r^2} \frac{\partial}{\partial r} (r^2 \frac{\partial}{\partial r})$. The scaling in eq. (10) uses the viscous diffusion timescale. The conventional scaling in geomagnetism uses the magnetic diffusion timescale, for which the coefficient of the last term in eq. (10) is the magnetic Reynolds number, the ratio of advection of magnetic field by the flow to magnetic field diffusion

$$R_m = \frac{UL}{\lambda}, \quad (11)$$

where U , L and λ are typical velocity, length and magnetic diffusivity, respectively. From the large-scale secular variation, $R_m \sim 500$ (Blokhin & Jackson 1991), so that advection is nominally larger than diffusion for large-scale flow in the core. This is the usual argument for using the frozen-flux approximation, in which both magnetic diffusion terms on the right-hand side of eq. (10) are neglected (Roberts & Scott 1965). Another reason for making the frozen-flux approximation is that, although the radial magnetic field on the core–mantle boundary is known from models of the main geomagnetic field (e.g. Jackson *et al.* 2000), its radial derivatives below the core–mantle boundary are unknown. Accordingly, we drop the first term on the right-hand side of eq. (10) in all cases. The second term on the right-hand side can be calculated from the magnetic field model, so in some cases we retain this term. In numerical dynamos the magnetic Reynolds number (eq. 11) can be written in terms of the magnetic Prandtl number P_m

$$R_m = U^* L^* P_m, \quad (12)$$

where the typical dimensionless dynamo velocity U^* is calculated by averaging the dynamo output in volume and time, the typical dimensionless length scale is the ratio of the outer core's radius to thickness $L^* = 1.54$, and the magnetic Prandtl number factors in the magnetic diffusivity. This quantity might be inappropriate, because the scale of the magnetic field may be smaller than the core's radius.

We, therefore, consider an additional quantity, the scale-dependent magnetic Reynolds number R_m^* , in which the length scale is derived from the magnetic field spectrum. Here we use $2\pi R / \bar{l}_B$ as a length scale, where the average magnetic harmonic is given in terms of the magnetic power spectrum $B_l^2(l)$ by

$$\bar{l}_B = \frac{\sum_l l B_l^2}{\sum_l B_l^2}. \quad (13)$$

The length scale derived from the magnetic field spectrum is about 1.5 times larger than L^* in the large-scale cases 1 and 2, and about 1.7 times smaller than L^* in the small-scale cases 3 and 4 (compare R_m and R_m^* in Table 1).

In our inversion method the tangential velocity is expressed in terms of a streamfunction Ψ and a scalar potential Φ as

$$\vec{u}_h = \nabla \times \Psi \hat{r} + \nabla_h \Phi, \quad (14)$$

where \hat{r} is the unit radial vector, and $\nabla_h = \nabla - \hat{r} \partial / \partial r$ in a spherical coordinate system (r, θ, ϕ) . Substitution of eq. (14) into eq. (10) and evaluation at $r = R$ yields

$$\begin{aligned} \frac{\partial B_r}{\partial t} + \frac{1}{R^2 \sin \theta} \left(\frac{\partial \Psi}{\partial \phi} \frac{\partial B_r}{\partial \theta} - \frac{\partial \Psi}{\partial \theta} \frac{\partial B_r}{\partial \phi} \right) \\ + \frac{1}{R^2} \left(\frac{\partial \Phi}{\partial \theta} \frac{\partial B_r}{\partial \theta} + \frac{1}{\sin^2 \theta} \frac{\partial \Phi}{\partial \phi} \frac{\partial B_r}{\partial \phi} \right) \\ + B_r \nabla_h^2 \Phi = \frac{1}{P_m} \left(\frac{1}{R^2} \frac{\partial^2}{\partial r^2} (r^2 B_r) + \nabla_h^2 B_r \right). \end{aligned} \quad (15)$$

We represent the tangential divergence of velocity by a superposition of the standard tangential geostrophy term (LeMouél 1984; Gire & LeMouél 1990; Jackson 1997; Hulot *et al.* 2002) plus a helical flow term

$$\nabla_h \cdot \vec{u}_h = \mp k \zeta + \frac{\tan \theta}{R} u_\theta. \quad (16)$$

The first term on the right-hand side of eq. (16) represents helical flow. Helical flow applies in situations where the tangential divergence is correlated with the radial vorticity ζ . The minus sign in eq. (16) applies to the Northern Hemisphere and the plus sign to the Southern Hemisphere. The second term on the right-hand side of eq. (16) represents tangential geostrophy. Substitution of eq. (14) into eq. (16) yields

$$\nabla_h^2 \Phi = \mp k \nabla_h^2 \Psi + \frac{\tan \theta}{R^2} \left(\frac{1}{\sin \theta} \frac{\partial \Psi}{\partial \phi} + \frac{\partial \Phi}{\partial \theta} \right). \quad (17)$$

The non-dimensional constant k is essentially a free parameter and describes the strength of helicity in the core. Analytical models of rotational flows and results from numerical dynamos suggest that $0.5 > k > 0.05$ (Amit & Olson 2004).

We solve eqs (15) and (17) simultaneously to obtain the potentials Ψ and Φ using a second-order, central finite-difference method on a regular spherical grid with radius R . Our method is identical to the one used by Amit & Olson (2006), and includes a special treatment of the equatorial region as a non-geostrophic belt. The numerical convergence of our method relies on positive effective streamfunction diffusivity; therefore, the sign of B_r in the helical flow upwelling term is reversed in areas of reverse magnetic flux (Amit & Olson 2004). In some solutions frozen flux is assumed and both terms on the right-hand side of eq. (15) are neglected, and in others the term representing tangential magnetic diffusion is included in the inversions. In geomagnetism, knowledge of the magnetic diffusivity is necessary in order to evaluate tangential magnetic diffusion. Here we accounted for tangential magnetic diffusion using the magnetic

Prandtl number appropriate to the corresponding numerical dynamo model.

We evaluate the convergence of our iterative method using two misfit measures. The areal-average deviation of the secular variation from its forward calculated value based on eq. (15), normalized by the areal-average secular variation, is defined as the secular variation misfit M_{sv} . Similarly, the areal-average deviation of eq. (17) from equality, normalized by the areal-average tangential divergence, is defined as the divergence misfit M_{div} . Those misfits are used to verify and quantify the convergence of the iterative inversion scheme.

4 STATISTICAL MEASURES OF THE FLOW RECOVERY

The quality of flow magnitude and pattern recovery is measured by statistical comparison between the imaged velocity \vec{u}_h and the dynamo velocity \vec{u}_h^* (hereafter we denote dynamo parameters with *). The quality of the magnitude fit is measured by the ratio of the areal-average imaged absolute velocity to the areal-average dynamo absolute velocity \vec{u}_h/\vec{u}_h^* , and also by the ratio of their maximum absolute velocities $|\vec{u}_h|_{\max}/|\vec{u}_h^*|_{\max}$. The quality of fit of the flow pattern is measured by the correlation coefficient (Rau *et al.* 2000)

$$c = \frac{\int \vec{u}_h \cdot \vec{u}_h^* dS}{\sqrt{\int \vec{u}_h \cdot \vec{u}_h dS \int \vec{u}_h^* \cdot \vec{u}_h^* dS}}, \quad (18)$$

where dS is an area element on the outer boundary. In addition, we use a new statistic that measures the pointwise quality of the flow recovery, defined by the areal-average absolute vector difference between the imaged and dynamo velocities, $|\vec{u}_h - \vec{u}_h^*|$, normalized by the areal-average sum of the same vectors:

$$p = 1 - \frac{\int |\vec{u}_h - \vec{u}_h^*| dS}{\int |\vec{u}_h + \vec{u}_h^*| dS}, \quad (19)$$

where p is the point recovery factor. The statistics (18) and (19) were calculated on the same grid used for calculating the imaged velocity.

Larger values of the correlation coefficient and the point recovery factor correspond to higher-quality flow recovery. Their values are the same in some limiting cases. For perfect recovery, $c = p = 1$. For zero imaged velocity, that is, the null case, $c = p = 0$, and for two random velocity fields, that is, $\vec{u}_h \perp \vec{u}_h^*$, $c = p = 0$. However, these two statistics are generally different, since c is a measure of pattern whereas p is also affected by the magnitude. For example, two velocity fields with identical pattern but with a magnitude difference, $\vec{u}_h = \alpha \vec{u}_h^*$ where $\alpha > 1$, result in $c = 1$ but $p = 2/(1 + \alpha)$.

Regional values of c and p can also be used to estimate the quality of fit in specific areas. For example, we define the regional correlation coefficient c_{ee} according to eq. (18) but excluding the 10° latitude band around the equator. Differences between values of c and c_{ee} indicate the contribution of the equatorial region to the recovery of the flow pattern.

5 FROZEN FLUX IN NUMERICAL DYNAMOS

Most core flow imaging methods assume frozen flux, justified by the large magnetic Reynolds number estimated from secular variation (Roberts & Scott 1965; Bloxham & Jackson 1991). The length scale of the flow is critical in this reasoning. Large-scale flow implies large R_m , that is, the diffusion timescale $\tau_\lambda = L^2/\lambda$ is much longer than the advection timescale $\tau_A = L/U$, and satisfies frozen flux,

and conversely small-scale flow implies diffusive effects that may bias the imaged velocity significantly. There is another condition for frozen flux that depends on the timescale over which the dynamo evolves. Gubbins & Kelly (1996) proposed that the timescale associated with core flow variations, $\tau_u = |\vec{u}|/|\partial\vec{u}/\partial t|$, must be smaller than the diffusion timescale and larger than the advection timescale for frozen flux to hold. Love (1999) argued that frozen flux is not expected to apply to a nearly steady dynamo because of the coupling of steady dynamo action and secular variation and the reliance of dynamo action on diffusion. Several different approaches for including diffusive effects in core flow imaging have been proposed (Voorhies 1993; Gubbins 1996; Love & Gubbins 1996), but not all the consequences of these approaches have been fully tested.

Because of these uncertainties, we have assessed the validity of the frozen-flux approximation in the numerical dynamo models used in this study. Fig. 1 shows the dynamo model secular variation and its advective and diffusive parts for case 1. The advective part was calculated using the dynamo velocity and radial magnetic fields, and the diffusive part is just the residual of the secular variation after the advective part has been removed. The advective part is generally larger and nearly equals the secular variation, whereas the diffusive part is secondary. Moreover, the advective part is highly correlated with the secular variation (the areal-average correlation between Figs 1(a) and (b) is 0.75), whereas the diffusive part is not (the areal-average correlation between Figs 1(a) and (c) is 0.01).

Another way to assess the validity of the frozen-flux approximation is to examine the timescales of the secular variation of different modes. The secular variation timescale for mode ℓ is given by (Hongre *et al.* 1998; Christensen & Tilgner 2004)

$$\tau_\ell = \sqrt{\left[\sum_{m=0}^n (g_{nm}^2 + h_{nm}^2) \right] / \left[\sum_{m=0}^n (\dot{g}_{nm}^2 + \dot{h}_{nm}^2) \right]}. \quad (20)$$

Table 2 summarizes the dynamo secular variation timescales for the studied cases. Table 2 also contains the poloidal free decay times for the first six modes (Gubbins & Roberts 1987). The dynamo dipole timescale is comparable to or smaller than the dipole free decay time, and all the other dynamo timescales ($\ell > 1$) are significantly smaller than the corresponding free decay times.

The results of Fig. 1 and Table 2 demonstrate that the dominant balance in the radial magnetic induction equation at the numerical dynamo models considered in this study is between secular variation and magnetic field advection by the flow, consistent with the frozen-flux approximation. Effects of magnetic field diffusion are expected to bias the imaged velocity to some extent, perhaps mostly locally, but the major changes in the radial magnetic field are due to advection as assumed by the frozen flux imaging method.

6 RESULTS

6.1 Testing helical flow

Our imaging technique differs from other methods in that it includes a helical flow term in the prescription of the tangential divergence (eq. 16). In order to determine how well the helical flow assumption captures the dynamics in the numerical dynamo models, we compare in Fig. 2 the tangential divergence and radial vorticity of the dynamo velocity and imaged velocity for case 1. The imaged velocity was obtained using $k = 0.1$ and includes tangential magnetic diffusion. According to the helical flow assumption, we expect the tangential divergence to be anticorrelated in the Northern Hemisphere and correlated in the Southern Hemisphere to the radial vorticity (eq. 16).

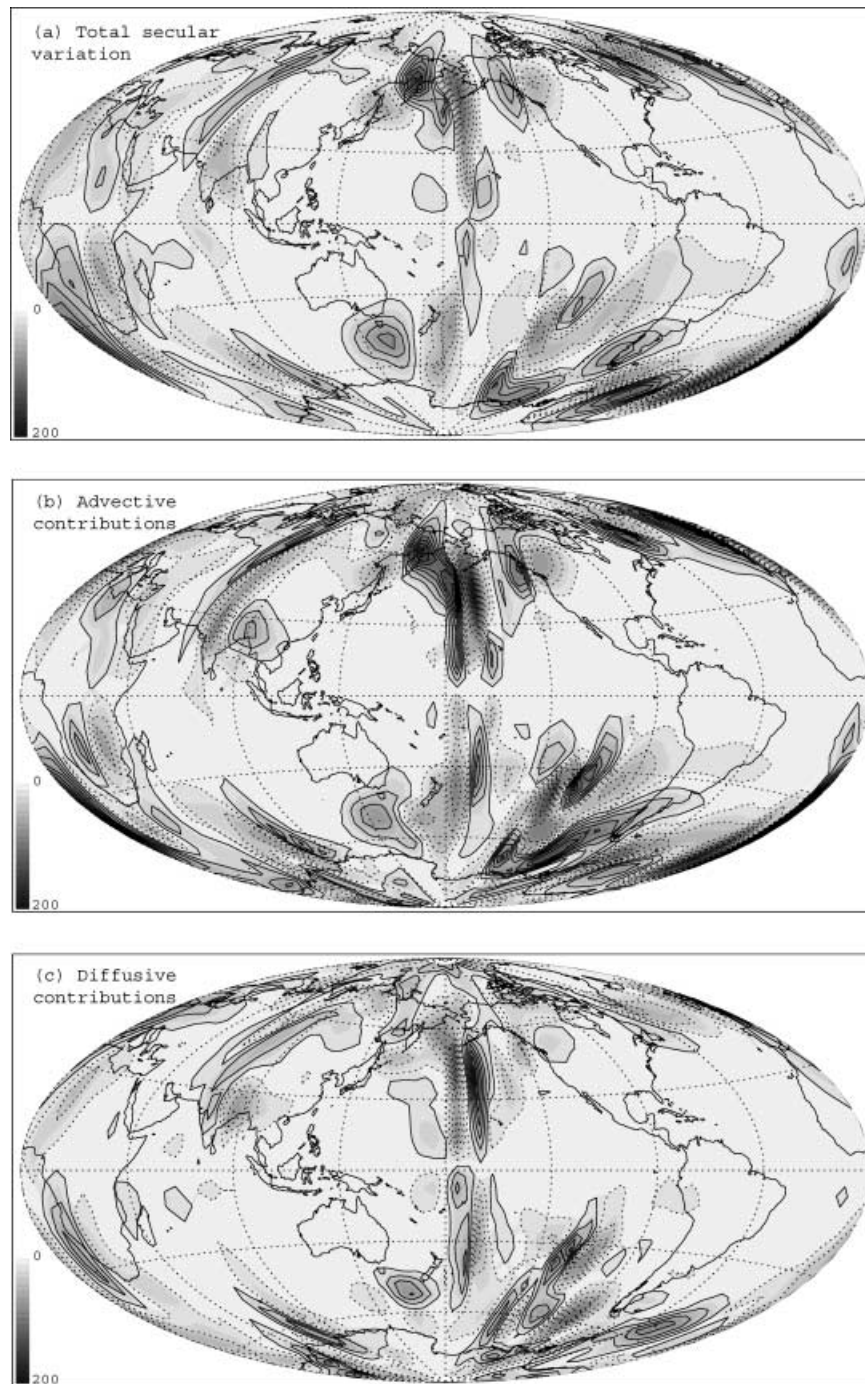


Figure 1. Total (a), advective contributions (b) and diffusive contributions (c) to the secular variation in the numerical dynamo case 1. Advective contributions were calculated based on the dynamo velocity and radial magnetic fields, and diffusive contributions are the difference between (a) and (b). The correlation between (a) and (b) is 0.75 and between (a) and (c) is 0.01. The grey scale represents absolute values, solid lines are positive and dotted lines are negative.

Figs 2(a) and (b) exhibit this correlation, a visual demonstration that helical flow is a good representation of dynamo model velocities, as was found by Olson *et al.* (2002). Numerically, the areal-average correlation between $\nabla_h \cdot \vec{u}_h^*$ and $\mp \zeta^*$ is $c_h^* = 0.83$ (see c_h^* values in Table 1 for the other cases). The imaged upwelling consists of helical flow and tangentially geostrophic parts (according to eq. 16), so Figs 2(c) and (d) are less well correlated. The areal-average correlation between $\nabla_h \cdot \vec{u}_h$ and $\mp \zeta$ is $c_h = 0.53$ (see c_h values in Table 3 for the other cases). The contribution from helical flow can be seen in the imaged velocity as well (compare Figs 2c and d).

Two additional points on Fig. 2 are worth-noting. First, the imaged radial vorticity (Fig. 2d) agrees with the dynamo radial vorticity (Fig. 2b), both in terms of pattern and magnitude. All major radial vorticity structures are present with the correct location and sign in the imaged radial vorticity, except for the negative vorticity structure below Scandinavia and some artefacts in the equatorial region. The radial vorticity pattern consists mostly of north–south narrowly elongated structures, alternately positive and negative. For example, below Central Asia, Figs 2(b) and (d) contain negative vorticity from India northwards and positive vorticity from

Table 2. Secular variation timescales of the dynamo models as a function of spherical harmonic degree ℓ calculated using eq. (20) as defined by Christensen & Tilgner (2004), in units of magnetic diffusion time magnified by 1000. Free decay times of the first six modes are given in the same units, based on a magnetic diffusivity of $\lambda = 1 \text{ m}^2 \text{ s}^{-1}$.

Case	τ_1	τ_2	τ_3	τ_4	τ_5	τ_6	τ_7	τ_8
1	122.93	12.55	16.75	8.03	10.65	5.23	4.94	4.07
2	263.43	17.95	28.40	12.20	17.94	7.50	7.51	5.92
3	55.45	3.21	4.55	2.39	3.03	1.64	1.49	1.30
4	49.35	3.86	4.52	2.72	2.87	1.78	1.62	1.40
Free decay	239.81	117.23	71.25	48.47	35.35	27.04		

Iran northwards. Even some non-columnar structures are recovered, for example the negative vorticity south of New Zealand (Figs 2b and d). In contrast, the imaged tangential divergence is consistently underestimated (note scales in Figs 2a and c) probably because the k -value assumed in the inversion is only about one third the actual value in the dynamo model ($k = 0.1$ versus $k^* = 0.31$, see Table 1).

The helical flow correlation in all dynamo models (c_h^* in Table 1) are generally high, especially for the large-scale dynamo velocities. Results of a linear regression between $\nabla_h \cdot \vec{u}_h^*$ and $\mp \zeta^*$ are also given (k^* in Table 1). Note that the k^* values for the lower Ekman number (more Earth like) cases tend towards the $k = 0.1$ used in our inversions. The helical flow correlation for all imaged velocity cases (c_h in Table 3) is also adequate, though less good than for the dynamo velocities, probably because the *a priori*-assumed model for the tangential divergence includes tangential geostrophy.

6.2 Large-scale dynamos

Fig. 3 shows the radial magnetic field and secular variation of case 1. The dynamo model magnetic field shares some similarity with the geomagnetic field on the core–mantle boundary, including dipolar dominance and intense flux concentrations at high latitudes. Also, the characteristic length scale of the secular variation is smaller than the length scale of the field itself, similar to the geomagnetic field on the core–mantle boundary (Hulot *et al.* 2002). However, there are some local morphological differences worth noting. The geomagnetic field in the equatorial region contains high-intensity normal polarity flux (Jackson 2003), whereas the dynamo magnetic field contains very low-intensity flux there (Fig. 3a).

Figs 4(a) and (b) show the dynamo velocity and the imaged velocity, respectively for case 1. The imaged velocity is obtained using $k = 0.1$ with tangential magnetic diffusion included. Due to the relatively low spatial resolution used in the dynamo model (see Table 1), a $5^\circ \times 5^\circ$ grid was deemed sufficient for the inversion. The statistics of this case are summarized in Table 3.

The dynamo velocity field is characterized by high-latitude vortices, strong meridional jets due to columnar convection, some equatorial symmetry, and a significant amount of flow along B_r -contours. Most of the main flow features in the dynamo velocity are also present in the imaged velocity. In the Northern Hemisphere, the vortices centred at $[170^\circ\text{E}, 52.5^\circ\text{N}]$ and $[225^\circ\text{E}, 42.5^\circ\text{N}]$ (Fig. 4a) appear with the correct position and direction of circulation in the imaged velocity (Fig. 4b). Northward jets at 5°W and 75°E and southward jets at 50°E and 300°E and most southern hemispheric main flow features are also well recovered. For example, the vortices centred at $[165^\circ\text{E}, 57.5^\circ\text{S}]$ and $[225^\circ\text{E}, 37.5^\circ\text{S}]$ are recovered by the imaged velocity both in terms of position and direction of

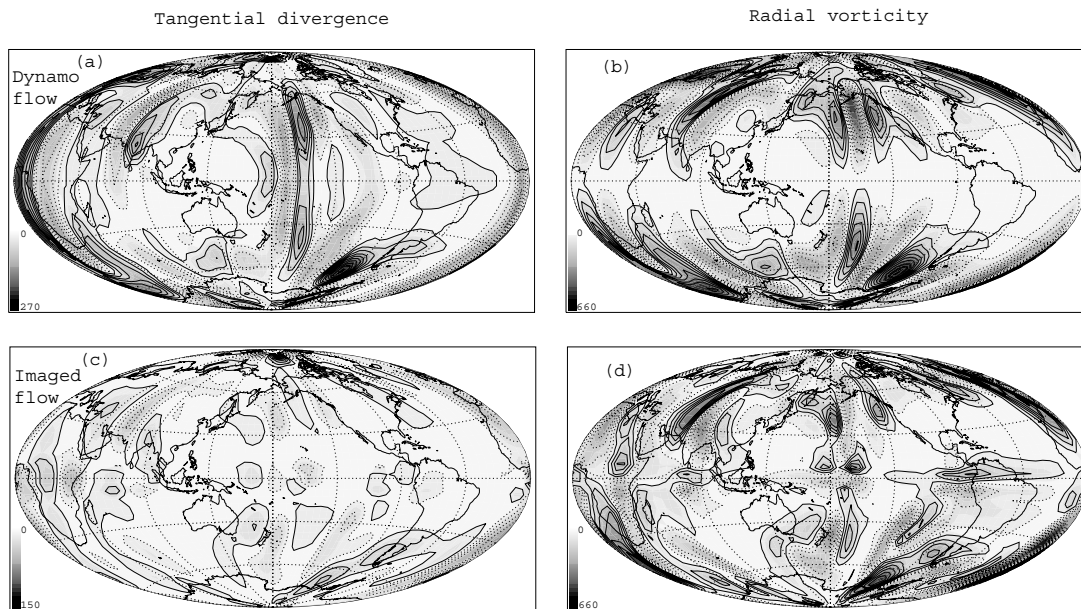


Figure 2. Relationships between tangential divergence and radial vorticity in case 1. The quantities derived from the dynamo velocity (a, b) are shown at depth $0.04D$ (where D is the shell thickness) below the outer boundary. The quantities derived from the imaged velocity (c, d) are calculated assuming $k = 0.1$ in eq. (16) for the helical flow and includes both tangential geostrophy and tangential magnetic diffusion. Note the difference in the scale bars in the tangential divergence maps. The correlation coefficient between tangential divergence (a) and \mp radial vorticity (b) in the dynamo velocity is 0.83, and the correlation between (b) and \mp (d) in the imaged velocity is 0.53, where the minus sign applies in the Northern Hemisphere and the plus sign applies in the Southern Hemisphere. Note that the correlation coefficient measures pattern agreement, not magnitude agreement. The grey scale represents absolute values, solid lines are positive and dotted lines are negative.

Table 3. Statistics of inversion tests. \vec{u}_h is the imaged velocity, \vec{u}_h^* is the dynamo velocity. $\|\cdot\|$ and \max denote absolute value and maximum, respectively. \bar{u} denotes the areal-average of \vec{u} . 2a and 2b are two different snapshots of the same simulation, f denotes filtered cases. c is the correlation coefficient defined in eq. (18), c_{ee} is the same coefficient excluding the 10° latitude band around the equator, p is the point recovery factor defined in eq. (19). M_{sv} and M_{div} are the secular variation and divergence misfits, respectively. The correlation coefficient between $\nabla_h \cdot \vec{u}_h$ and $\mp \zeta$ is c_h .

Case	k	$\nabla_h^2 B_r$	$ \vec{u}_h _{\max}/ \vec{u}_h^* _{\max}$	\vec{u}_h/\vec{u}_h^*	c	c_{ee}	p	M_{sv} per cent	M_{div} per cent	c_h
1	0.1	no	0.80	0.71	0.46	0.53	0.34	0.2	2.7	0.55
1	0.07	no	1.05	0.86	0.46	0.52	0.35	0.2	4.1	0.41
1	0.05	no	1.35	1.03	0.43	0.49	0.34	0.3	5.7	0.30
1	0.1	yes	0.90	0.79	0.51	0.59	0.40	0.7	2.8	0.53
2a	0.1	no	0.85	0.76	0.25	0.28	0.23	2.42	5.42	0.46
2a	0.1	yes	0.74	0.76	0.48	0.56	0.40	0.47	3.22	0.48
2b	0.1	no	0.79	0.53	0.31	0.38	0.23	1.85	1.93	0.42
2b	0.1	yes	0.91	0.64	0.52	0.64	0.42	0.25	2.22	0.45
3	0.1	no	1.58	0.97	0.21	0.24	0.21	1.61	3.44	0.34
3f	0.1	no	2.48	1.49	0.20	0.22	0.18	0.12	4.26	0.26
3	0.1	yes	1.53	0.99	0.23	0.28	0.23	1.87	3.01	0.34
4	0.1	no	2.28	1.04	0.07	0.10	0.10	1.64	3.62	0.40
4f	0.1	no	3.94	1.90	-0.01	-0.02	0.03	2.08	4.20	0.28
4	0.1	yes	2.13	1.02	0.10	0.11	0.14	1.82	3.23	0.41

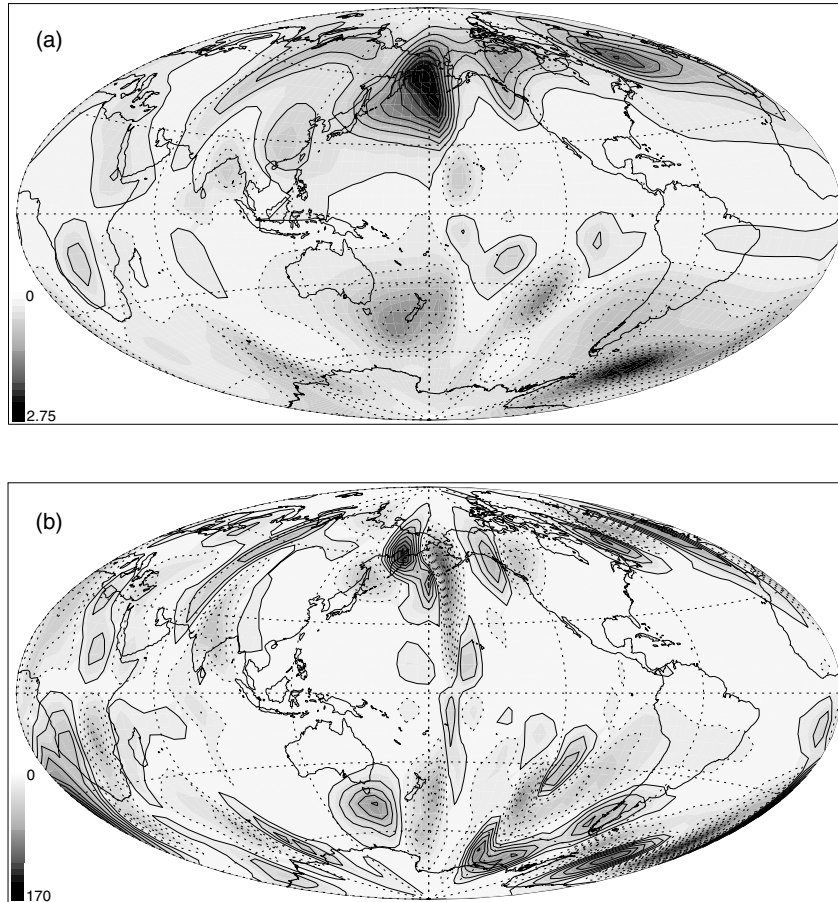


Figure 3. Radial magnetic field (a) and secular variation (b) on the outer boundary for case 1. The grey scale represents absolute values, solid lines are positive and dotted lines are negative.

circulation. The vortex centred at $[265^\circ\text{E}, 57.5^\circ\text{S}]$ in the dynamo velocity is shifted by about 10° to the southwest in the imaged velocity.

However, in some places the inversion fails to recover the dynamo velocity. For example, the anticyclonic vortex centred at $[15^\circ\text{E}, 57.5^\circ\text{N}]$ is not found in the imaged velocity. Also, between longitudes 50°E – 75°E the meridional jets in the imaged velocity

connect by an eastward flow at latitudes 17.5°N – 37.5°N , whereas in the dynamo velocity this region exhibits a shear flow. Flow in the polar regions is generally poorly recovered.

The dynamo velocity in the equatorial region is very weak (Fig. 4a). Nevertheless, the inversion predicts some flow and shear in that region, mostly zonal (Fig. 4b). Olson *et al.* (1999) found that the zonal displacement of magnetic flux at low latitudes is not

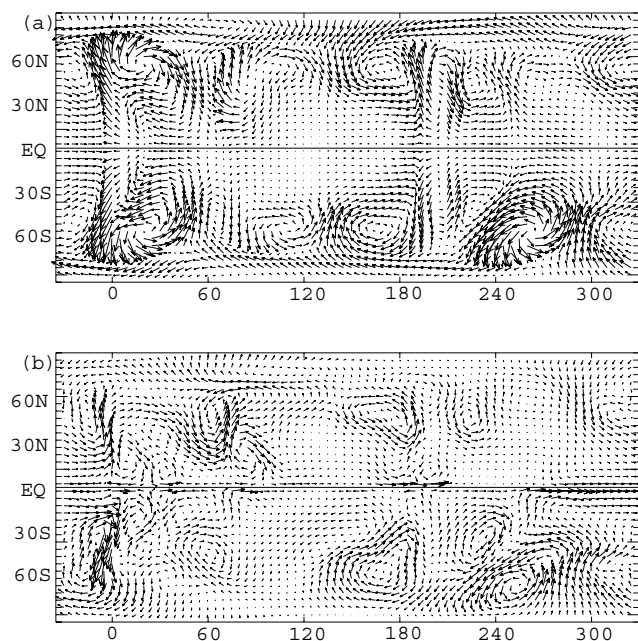


Figure 4. dynamo velocity (a) and imaged velocity (b) for case 1 with $k = 0.1$ and tangential magnetic diffusion. Maximum velocity in (a) is 100.0, and velocity arrows in (b) are scaled according to (a).

always due to zonal flow, but sometimes due to magnetic diffusion effects. Similar interpretation to equatorial flow artefacts was given by Rau *et al.* (2000).

Previously used physical assumptions for the tangential divergence of the flow do not solve the problem of non-uniqueness completely. Toroidal flows are non-unique along B_r -contours (Whaler 1980), and tangential geostrophic flows are non-unique along $B_r/\cos\theta$ -contours (where θ is co-latitude) that do not cross the equator (Backus & LeMouél 1986; Bloxham & Jackson 1991). A standard damped least-squares solution minimizes the null-space vector contribution to the flow solutions (Gubbins 2004). Our helical flow assumption removes non-uniqueness; there is no null-space vector in our inversions (Amit & Olson 2004). Even along $B_r/\cos\theta$ -contours, some secular variation is produced by the helical flow upwelling. Some of the main flow features in the dynamo velocity contain significant flow along B_r -contours (Rau *et al.* 2000; Olson *et al.* 2002), and these flow components are well recovered by the imaged velocity. For example, the main magnetic field structure in the Northern Hemisphere is a large and intense normal flux located between longitudes 140°E – 195°E and between latitudes 30°N – 70°N (Fig. 3a). The dynamo velocity at that area is a cyclonic vortex with a significant flow component along B_r -contours (Fig. 4a). This vortex is well represented in the imaged velocity (Fig. 4b). Note that the eastern margin of the magnetic flux structure is oriented north–south and coincides with the northward jet in both dynamo and imaged velocities.

Magnetic diffusion effects are relatively larger in the fully resolved magnetic fields of dynamo models than they are for the geomagnetic field truncated to a moderate spherical harmonic degree. In geomagnetic core flow inversions, the full magnetic diffusion effect cannot be considered because the geomagnetic field is only known over the core–mantle boundary, and its radial variation is unknown. However, the tangential part of magnetic diffusion can be calculated. We have examined the effects of tangential magnetic diffusion on the quality of flow recovery by comparing inversions with and with-

out the second term on the right-hand side of eq. (15). Including tangential magnetic diffusion has improved the imaged velocity; the correlation coefficient has improved from 0.46 to 0.51, and the point recovery factor has improved from 0.34 to 0.40 (Table 3). These improvements are not very large, probably because effects of tangential magnetic diffusion are typically smaller than effects of radial magnetic diffusion (Olson & Amit 2006). Nevertheless, they are statistically significant because they appear consistently in all cases (see Table 3). If tangential magnetic diffusion was balanced by radial magnetic diffusion, it would be expected that including only the tangential part would result in decreasing correlations. The improved recoveries in cases with tangential magnetic diffusion, therefore, suggest that tangential and radial magnetic diffusion contributions to the secular variation are spatially uncorrelated.

The choice of the non-dimensional parameter k mostly affects the magnitude of the imaged velocity, and can be ‘tuned’ to fit the magnitude of the dynamo velocity. The true value of k is unknown in the core. Amit & Olson (2004) used analytical models of simple rotating flows to infer the likely range of k in the core, and found that $0.5 > k > 0.05$ is typical. Here we use $k = 0.1$ in most cases, although we acknowledge that this parameter is spatially heterogeneous and depends on the other dynamo parameters. We do so in order to truly test real conditions; in the numerical dynamo models k^* may vary, depending on the model parameters (Table 1). Spectral methods ‘tune’ the damping parameter to fit best both the magnitude and the scale of the flow. In contrast to the damping parameter, the choice of k does not degrade our data misfits. Our method minimizes the data misfits and reaches optimal numerical convergence. The remaining data misfit is due to the complexity of the true relation between toroidal to poloidal flows that is not fully captured by the simplified physical assumption for the tangential divergence, and due to secular variation contamination by magnetic diffusion effects. Our inversions contain relative data misfits of less than 6 per cent, whereas the ones obtained by Rau *et al.* (2000) using spectral methods contain relative data misfits in the range 15–65 per cent.

Based on qualitative identification of flow features and some global statistics, the flow recovery in case 1 seems to be successful. The correlation coefficient which is a measure of the fit in terms of flow pattern is adequate, with $c = 0.51$ for the case with tangential magnetic diffusion (Table 3). The success of fit according to the point recovery factor p is slightly less good, $p = 0.4$ for the same case. Note that the two statistical measures are in some agreement in a sense that cases with relatively high/low c value also have relatively high/low p value.

In the second large-scale dynamo case 2 the magnetic Reynolds number is lower than in case 1. Fig. 5 shows the radial magnetic field and secular variation of case 2a. As in case 1, the magnetic field morphology is dominantly dipolar. Figs 6(a) and (b) show the true dynamo velocity and the imaged velocity for case 2a, respectively. The imaged velocity is obtained using $k = 0.1$ with tangential magnetic diffusion included. Because of the lower magnetic Reynolds number, effects of diffusion are much stronger here than in case 1. Indeed, the improvement in the quality of recovery by accounting for tangential magnetic diffusion is remarkable in case 2. For two different snapshots of the same case, 2a and 2b, including tangential magnetic diffusion has improved the correlation coefficient from 0.25 to 0.48 and from 0.31 to 0.52 respectively. The improvement is also evident in the point recovery factor, from 0.23 to 0.40 in case 2a, and from 0.23 to 0.42 in case 2b (table 3). The inversions of cases 2a and 2b without tangential magnetic diffusion are less successful than case 1, but with tangential magnetic diffusion the recoveries are comparable.

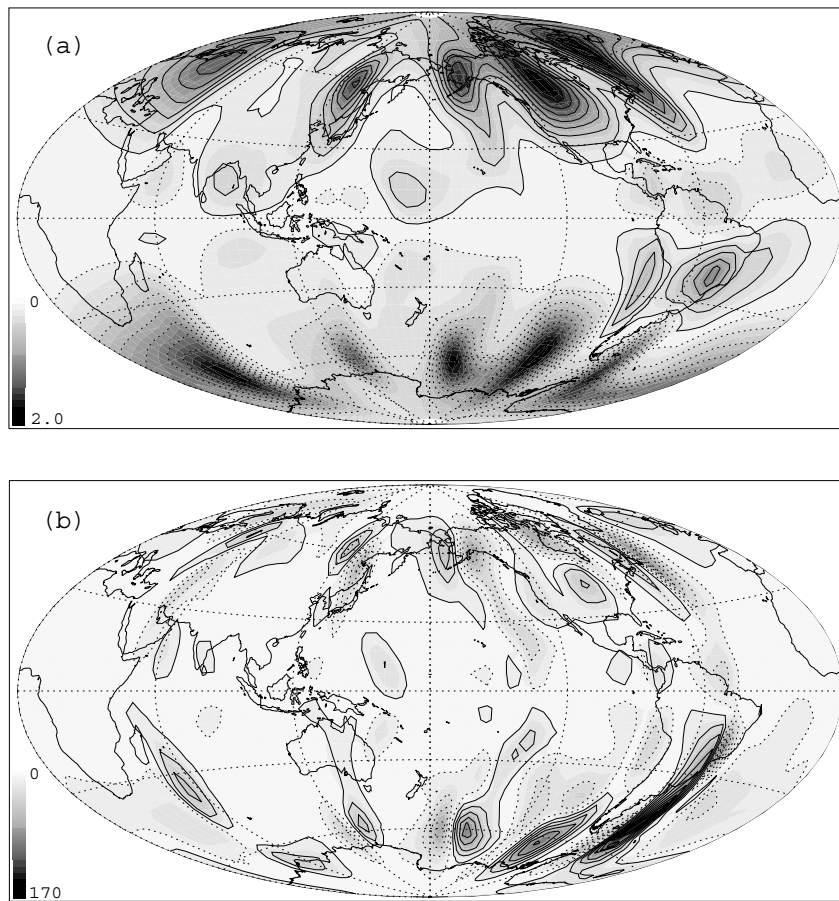


Figure 5. Radial magnetic field (a) and secular variation (b) on the outer boundary for case 2. The grey scale represents absolute values, solid lines are positive and dotted lines are negative.

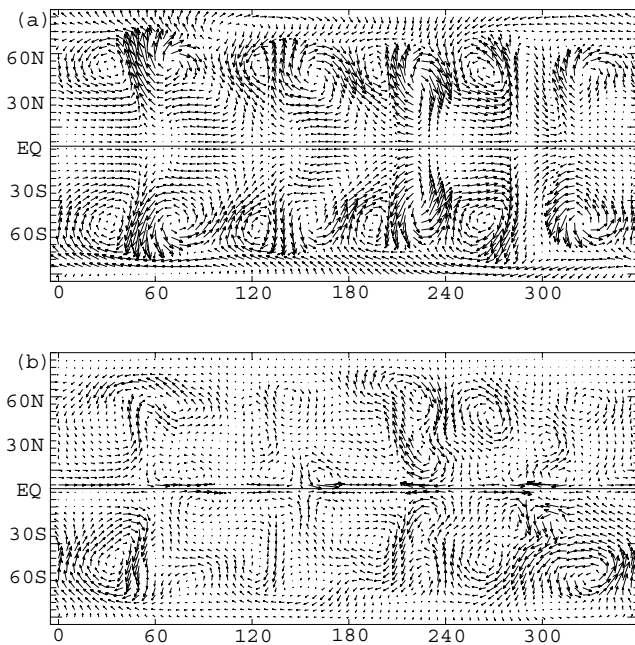


Figure 6. dynamo velocity (a) and imaged velocity (b) for case 2a with $k = 0.1$ and tangential magnetic diffusion. Maximum velocity in (a) is 79.7, and velocity arrows in (b) are scaled according to (a).

The quality of the flow recovery is degraded in the equatorial region, where (1) effects of radial magnetic diffusion are large and (2) our inversion method is weak due to the reverse flux patches in numerical dynamos there. We repeated the calculation of the correlation coefficient, this time excluding the 10° low latitudes from the integration in eq. (18) (see c_{ee} values in Table 3). For example, case 2b with tangential magnetic diffusion has a correlation coefficient of $c = 0.52$. Excluding the band $\pm 10^\circ$ around the equator gives $c_{ee} = 0.64$ for this case (Table 3), and excluding the lowest 30° latitudes gives 0.71 (not shown in Table). Clearly, the flow recovery is adequate at mid- and high latitudes where most of the intense flow structures are present in the dynamo velocity. The recovery is substantially degraded at low latitudes due to strong radial magnetic diffusion effects, the singularity of the tangential geostrophy, and methodological problems of our inversion there.

These cases demonstrate that overall, properties of the large-scale flow are well recovered, both in magnitude and in pattern. The quality of fit is better in terms of magnitude and comparable in terms of pattern with respect to the quality of fits obtained by Rau *et al.* (2000). Most main flow features in the dynamo velocity are present in the imaged velocity at the correct position and with the correct direction of circulation.

6.3 Small-scale dynamos

Fig 7 and 9 show the radial magnetic field and secular variation of cases 3 and 4, respectively. The heat flux is imposed on the outer

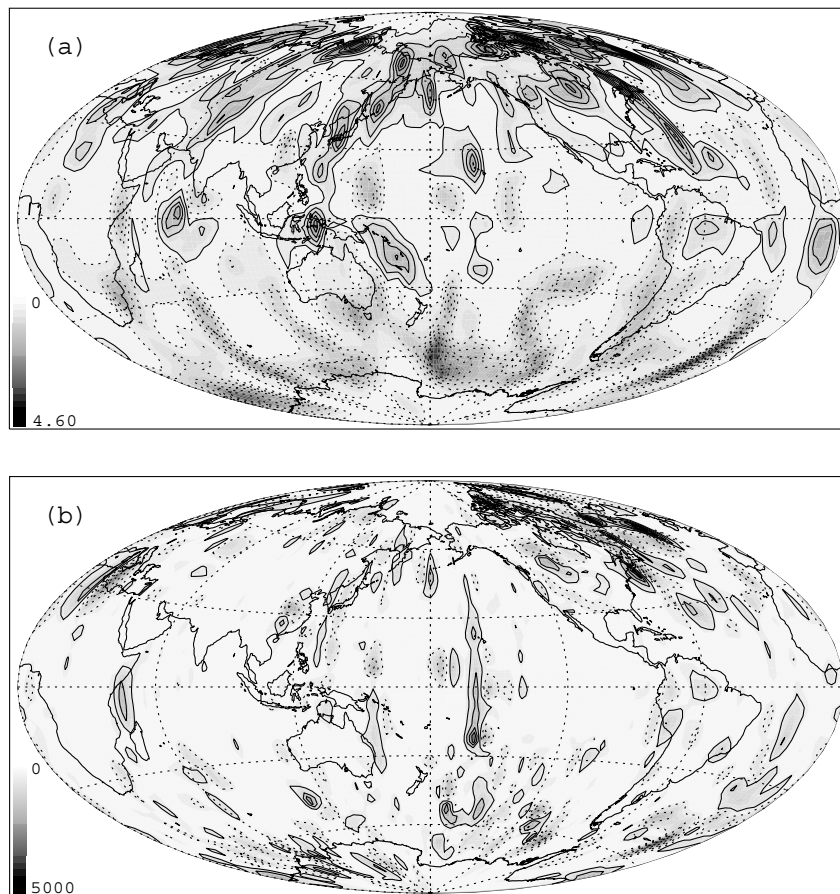


Figure 7. Radial magnetic field (a) and secular variation (b) on the outer boundary for case 3. The grey scale represents absolute values, solid lines are positive and dotted lines are negative.

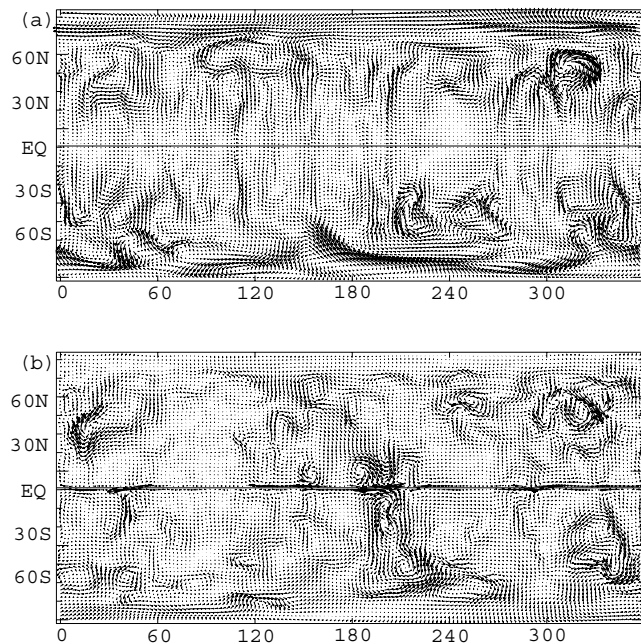


Figure 8. dynamo velocity (a) and imaged velocity (b) for case 3 with $k = 0.1$ and tangential magnetic diffusion. Maximum velocity in (a) is 879.1, and velocity arrows in (b) are scaled according to (a).

boundary, uniform in case 3 and with a heterogeneous pattern obtained from a lower mantle tomography model (Masters *et al.* 1996; Olson & Christensen 2002) in case 4. With larger Rayleigh number and smaller Ekman number than cases 1 and 2 (see Table 1), more vigorous convection and stronger rotational effects produce smaller-scale velocity fields in these cases. The larger magnetic Reynolds number also reduces the scale of the magnetic field in these dynamos. As in cases 1 and 2, the magnetic field is dominantly dipolar but includes much smaller spatial scales of variation (see Figs 7 and 9), necessitating a finer grid ($2.5^\circ \times 2.5^\circ$) for the inversions.

Figs 8 and 10 compare the dynamo and imaged velocities for cases 3 and 4, respectively. The imaged velocities were obtained using $k = 0.1$ with tangential magnetic diffusion included. The statistics of cases 3 and 4 is summarized in Table 3. As in cases 1 and 2, including tangential magnetic diffusion improves the quality of the flow pattern. In case 3 the correlation coefficient improves from 0.21 to 0.23, and in case 4 from 0.07 to 0.10 (Table 3). However, the quality of the flow recovery is much lower than in cases 1 and 2, with correlation coefficients between 0.10 to 0.23 and point recovery factors between 0.14 and 0.23. The larger magnetic Reynolds number R_m in cases 3 and 4 (Table 1) may suggest that magnetic diffusion effects are weaker in these cases. However, the scale-dependent magnetic Reynolds number R_m^* remains nearly constant in all cases, indicating the importance of magnetic diffusion in the more complex dynamos. Some of the diffusive effects may be captured by including tangential magnetic diffusion, but much of the signal is likely the result of

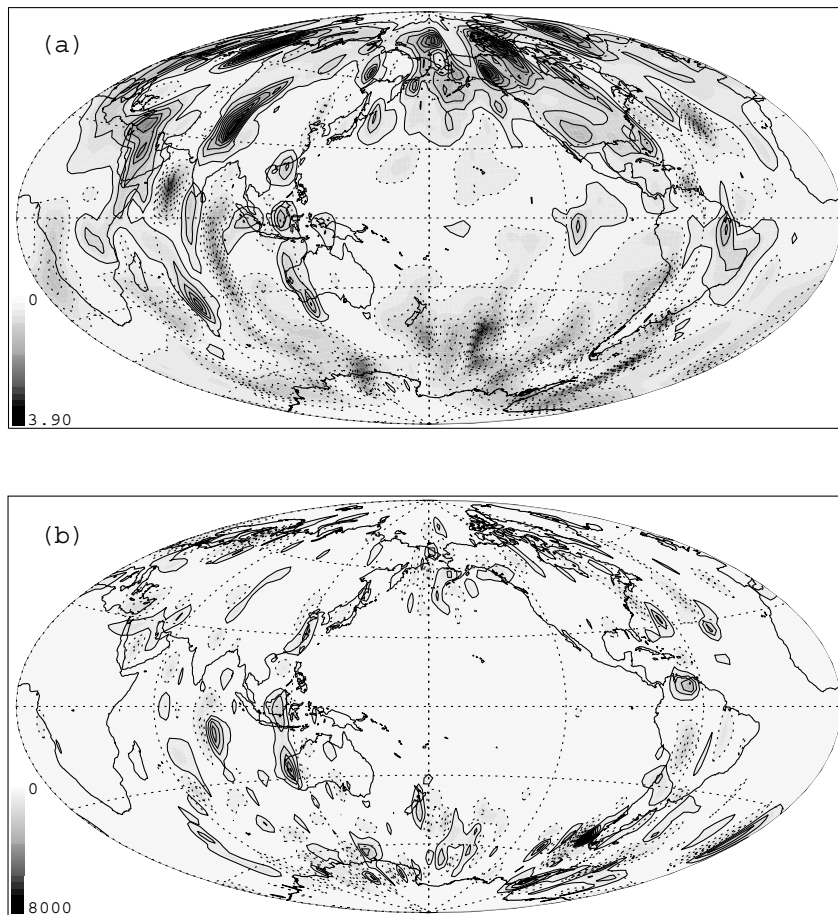


Figure 9. Radial magnetic field (a) and secular variation (b) on the outer boundary for case 4. The grey scale represents absolute values, solid lines are positive and dotted lines are negative.

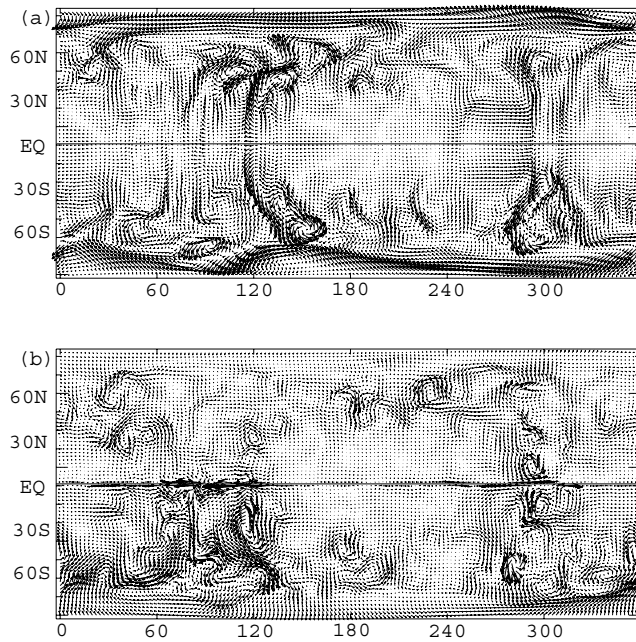


Figure 10. dynamo velocity (a) and imaged velocity (b) for case 4 with $k = 0.1$ and tangential magnetic diffusion. Maximum velocity in (a) is 753.3, and velocity arrows in (b) are scaled according to (a).

radial diffusion, which we do not model. For this reason, the quality of inversions with smaller-scale secular variation is significantly lower than for the large-scale cases 1 and 2.

Some of the problems in recovering complex flow from small-scale secular variation are illustrated by the intense flow structure in the imaged velocity of case 3 in the equatorial region at about longitude 180°E (Fig. 8b). There is no corresponding structure in the dynamo velocity (Fig. 8a) although there is a significant secular variation at this location (Fig. 7b). Because the magnetic field is weak (see Fig. 7a), tangential magnetic diffusion cannot be the major source of secular variation. More likely radial magnetic diffusion causes local rapid changes in the radial magnetic field at this area and results in a flow artefact.

Despite the problems of imaging small-scale velocity structures, case 3 succeeds in recovering several of the main flow features. The most intense flow feature in the dynamo model is an anticyclonic vortex centred at about $[310^\circ\text{E}, 45^\circ\text{N}]$ (Fig. 8a). This structure is well recovered in position and direction of circulation, and it is one of the most intense flow features in the dynamo and in the imaged velocities (Fig. 8b). More examples of successful flow recoveries include the intense cyclonic vortex centred at about $[215^\circ\text{E}, 50^\circ\text{S}]$ and equatorially symmetric poleward jets at about longitude 345°E . The quality of flow recovery in case 4 is lower than in case 3, probably because the tomographic boundary conditions induce a more complex smaller-scale dynamo velocity.

Hulot *et al.* (1991) showed that effects of magnetic data truncation may lead to errors in core flow inversions. We tested the effects of

magnetic field truncation on core flow recovery in cases 3f and 4f. We used the same magnetic field and secular variation data as before, but this time we applied a low-pass filter to both the magnetic field and secular variation data prior to inversion. The low-pass filter is a cosine function centred at spherical harmonic degree $l = 12$ with a width $w = 2$, so features represented by $l = 10$ are unchanged, those for $l = 12$ are moderately truncated, and for $l \geq 14$ are completely removed. The imaged velocity obtained by inverting the filtered secular variation is then compared with the dynamo velocity that was also filtered in the same way. The statistics of the filtered cases are given in Table 3 (cases 3f and 4f). We find that the inversions of the filtered cases are degraded in quality of flow recovery with respect to the corresponding non-filtered cases, in the same ways found by Rau *et al.* (2000).

The poor recovery in the inversions of small-scale dynamo fields is probably due to the local effects of radial magnetic diffusion and the complexity of the secular variation, rather than insufficient numerical resolution. Paradoxically, although the more complex dynamos have nominally higher R_m values, they are actually more diffusive, which accounts for the reduction in the quality of our flow images. A better measure of the relative contributions of advection and diffusion to the secular variation is based on the characteristic length scale of the field from its energy spectrum. We find that the scale-dependent magnetic Reynolds number R_m^* based on this length scale (13) is nearly constant for all cases. In the larger-scale cases the pointwise ratio of advection to diffusion of magnetic field is more uniformly distributed, whereas in the smaller-scale cases this ratio is more heterogeneous, resulting in some localities where large radial magnetic diffusion effects contribute significantly to the secular variation and flow artefacts there. We conclude that unmodelled local effects of radial magnetic diffusion in small-scale dynamos with vigorous convection, especially in the equatorial region, degrade the flow recovery.

Our inversions of small-scale dynamo velocities are less successful in terms of the correlation coefficient (18) in comparison with similar cases inverted by Rau *et al.* (2000) because of the flexibility of spectral methods in the choice of the damping parameter. The choice of damping parameter creates a trade-off between data misfits and flow scale, and allows for large data misfits that absorb magnetic diffusion effects (see table 2 of Rau *et al.* 2000). These large data misfits are useful when the true flow is known, but would not be used in geomagnetic secular variation inversions where the typical misfit is less than 10 per cent (e.g. Bloxham 1989). Our method does not *a priori* select the flow scale or the data misfits, but instead minimizes the data misfits locally on the grid.

7 CONCLUSIONS

We have introduced several new statistical measures of flow image quality, including the point recovery factor and the regional correlation coefficient. These measures, together with previous measures used by Rau *et al.* (2000), provide a more complete statistical analysis of the flow recovery. Tests of our frozen flux imaging using dynamo model flows reveals both strong and weak aspects of the method. We find that the magnitude of the imaged flow agrees with the true flow magnitude at the 80 per cent level. Different k -values affect the magnitude of the flow without increasing the inversion misfits. The overall flow pattern recovery is good in terms of capturing major flow structures, but their locations are often displaced, resulting in decreased spatial correlation. The helical flow assumption captures major vortex structures, both in terms of location and

direction of circulation. Including tangential magnetic diffusion improves the flow recovery, but unmodelled effects of radial magnetic diffusion degrade the flow recovery.

Inversions of secular variation from small-scale dynamos are significantly less successful than those of large-scale dynamos, probably due to the complexity of the secular variation. Poor recovery is especially found near the equator, where the tangential geostrophy and helical flow assumptions are violated and effects of radial magnetic diffusion are strong. In addition, effects of data truncation decrease image quality. Inversions of secular variation data filtered so as to account for the effects of crustal magnetization on the core field result in lower correlations than inversions using the same data unfiltered. Taken together, these two findings indicate that a prime objective for better images of the core flow is to improve secular variation models at large spherical harmonic degree.

ACKNOWLEDGMENTS

This research was supported by a grant from the Geophysics Program of the National Science Foundation. We thank two anonymous reviewers for their constructive suggestions. H.A. thanks the Max-Planck-Institut für Sonnensystemforschung for the generous hosting.

REFERENCES

- Amit, H. & Olson, P., 2004. Helical core flow from geomagnetic secular variation, *Phys. Earth Planet. Inter.*, **147**, 1–25, doi:10.1016/j.pepi.2004.02.006.
- Amit, H. & Olson, P., 2006. Time-average and time-dependent parts of core flow, *Phys. Earth Planet. Inter.*, **155**, 120–139, doi:10.1016/j.pepi.2005.10.006.
- Backus, G.E. & LeMouél, J.-L., 1986. The region on the core mantle boundary where a geostrophic velocity field can be determined from frozen flux magnetic data, *Geophys. J. R. astr. Soc.*, **85**, 617–628.
- Bloxham, J., 1989. Simple models of fluid flow at the core surface derived from geomagnetic field models, *Geophys. J. Int.*, **99**, 173–182.
- Bloxham, J. & Jackson, A., 1991. Fluid flow near the surface of Earth's outer core, *Rev. Geophys.*, **29**, 97–120.
- Christensen, U. & Tilgner, A., 2004. Power requirement of the geodynamo from ohmic losses in numerical and laboratory dynamos, *Nature*, **429**, 169–171.
- Christensen, U., Olson, P. & Glatzmaier, G.A., 1999. Numerical modeling of the geodynamo: a systematic parameter study, *Geophys. J. Int.*, **138**, 393–409.
- Gire, C. & LeMouél, J.-L., 1990. Tangentially geostrophic flow at the core-mantle boundary compatible with the observed geomagnetic secular variation: The large-scale component of the flow, *Phys. Earth Planet. Inter.*, **59**, 259–287.
- Gire, C., LeMouél, J.-L. & Madden, T., 1986. Motions of the core surface derived by SV data, *Geophys. J. R. astr. Soc.*, **84**, 1–29.
- Gubbins, D., 1996. A formalism for the inversion of geomagnetic data for core motions with diffusion, *Phys. Earth Planet. Inter.*, **98**, 193–206.
- Gubbins, D., 2004. *Time Series Analysis and Inverse Theory for Geophysicists*, Cambridge University Press, Cambridge.
- Gubbins, D. & Kelly, P., 1996. A difficulty with using the frozen flux hypothesis to find steady core motions, *Geophys. Res. Lett.*, **23**, 1825–1828.
- Gubbins, D. & Roberts, P.H., 1987. Magnetohydrodynamics of the Earth's core, in *Geomagnetism*, Vol. 2, chap. 1, ed. Jacobs, J.A., Academic, San Diego, CA.
- Holme, R. & Whaler, K.A., 2001. Steady core flow in an azimuthally drifting reference frame, *Geophys. J. Int.*, **145**, 560–569.

- Hongre, L., Hulot, G. & Khokhlov, A., 1998. An analysis of the geomagnetic field over the past 2000 years, *Phys. Earth Planet. Inter.*, **106**, 311–335.
- Hulot, G., LeMouél, J.-L. & Wahr, J., 1991. Taking into account truncation problems and geomagnetic model accuracy in assessing computed flows at the core-mantle boundary, *Geophys. J. Int.*, **108**, 224–246.
- Hulot, G., Eymin, C., Langlais, B., Mandea, M. & Olsen, N., 2002. Small-scale structure of the geodynamo inferred from Oersted and Magsat satellite data, *Nature*, **416**, 620–623.
- Jackson, A., 1997. Time-dependency of tangentially geostrophic core surface motions, *Phys. Earth Planet. Inter.*, **82**, 167–183.
- Jackson, A., 2003. Intense equatorial flux spots on the surface of the Earth's core, *Nature*, **424**, 760–763.
- Jackson, A., Bloxham, J. & Gubbins, D., 1993. Time-dependent flow at the core surface and conservation of angular momentum in the coupled core-mantle system, in *Dynamics of Earth's deep interior and Earth rotation*, *Geophysical Monograph 72 IUGG*, Vol. 12, pp. 97–107, eds LeMouél, J.-L., Smylie, D.E. & Herring, T.
- Jackson, A., Jonkers, A.R.T. & Walker, M.R., 2000. Four centuries of geomagnetic secular variation, *Phil. Trans. R. Soc. Lond., A*, **358**, 957–990.
- LeMouél, J.-L., 1984. Outer core geostrophic flow and secular variation of Earth's magnetic field, *Nature*, **311**, 734–735.
- Love, J.J., 1999. A critique of frozen-flux inverse modelling of a nearly steady geodynamo, *Geophys. J. Int.*, **138**, 353–365.
- Love, J.J. & Gubbins, D., 1996. Optimized kinematic dynamos, *Geophys. J. Int.*, **124**, 787–800.
- Masters, G., Johnson, S., Laske, G. & Bolton, H., 1996. A shear-velocity model of the mantle, *Phil. Trans. R. Soc. Lond., A*, **354**, 1385–1411.
- Olson, P. & Amit, H., 2006. Changes in Earth's dipole, *Naturwissenschaften*, **93**, doi:10.1007/s00114-006-0138-6.
- Olson, P. & Christensen, U.R., 2002. The time averaged magnetic field in numerical dynamos with nonuniform boundary heat flow, *Geophys. J. Int.*, **151**, 809–823.
- Olson, P., Christensen, U.R. & Glatzmaier, G.A., 1999. Numerical modeling of the geodynamo: mechanisms of field generation and equilibration, *J. geophys. Res.*, **104**, 10 383–10 404.
- Olson, P., Sumita, I. & Aurnou, J., 2002. Diffusive magnetic images of upwelling patterns in the core, *J. geophys. Res.*, **107**, doi:10.1029/2001jb000384.
- Pais, A. & Hulot, G., 2000. Length of day decade variations, torsional oscillations and inner core superrotation: evidence from recovered core surface zonal flows, *Phys. Earth planet. Inter.*, **118**, 291–316.
- Rau, S., Christensen, U., Jackson, A. & Wicht, J., 2000. Core flow inversion tested with numerical dynamo models, *Geophys. J. Int.*, **141**, 485–497.
- Roberts, P.H. & Scott, S., 1965. On analysis of the secular variation, 1, A hydromagnetic constraint: Theory, *J. Geomagn. Geoelectr.*, **17**, 137–151.
- Voorhies, C.V., 1986. Steady flows at the top of Earth's core derived from geomagnetic field models, *J. geophys. Res.*, **91**, 12 444–12 466.
- Voorhies, C.V., 1993. Geomagnetic estimates of steady surficial core flow and flux diffusion: unexpected geodynamo experiments, in *Dynamics of Earth's deep interior and Earth rotation*, *Geophysical Monograph 72 IUGG*, Vol. 12, pp. 113–125, eds LeMouél, J.-L., Smylie, D.E. & Herring, T.
- Whaler, K.A., 1980. Does the whole of Earth's core convect?, *Nature*, **287**, 528–530.